Journal of Colloid and Interface Science 561 (2020) 358–371

Contents lists available at ScienceDirect

Journal of Colloid and Interface Science

journal homepage: www.elsevier.com/locate/jcis

Polyol assisted formaldehyde reduction of bi-metallic Pt-Pd supported *agro-waste* derived carbon spheres as an efficient electrocatalyst for formic acid and ethylene glycol oxidation

Palanisamy Rupa Kasturi [a], Ramasamy Harivignesh [b], Yun Sung Lee [b], Ramakrishnan Kalai Selvan [a,*]

[a] Energy Storage and Conversion Devices Laboratory, Department of Physics, Bharathiar University, Coimbatore 641046, Tamil Nadu, India
[b] Faculty of Applied Chemical Engineering, Chonnam National University, Gwangju 500-757, South Korea

GRAPHICAL ABSTRACT

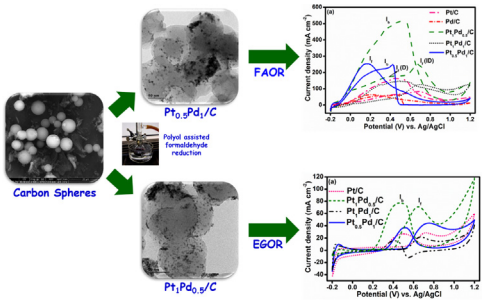

ARTICLE INFO

Article history:
Received 9 August 2019
Revised 28 October 2019
Accepted 31 October 2019
Available online 2 November 2019

Keywords:
Carbon spheres
Pt-Pd NPs decoration
Electrocatalyst
Formic acid oxidation
Ethylene glycol oxidation

ABSTRACT

This report explains, (i) the preparation of carbon spheres (CS) from *agro-waste* through hydrothermal carbonization (HTC) followed by high temperature carbonization, (ii) the decoration of bi-metallic Pt-Pd nanoparticles (Pt-Pd NPs) with different compositions (Pt/C, $Pt_{0.5}Pd_1$/C, Pt_1Pd_1/C and $Pt_1Pd_{0.5}$/C, Pd/C) on the carbon by ethylene glycol solvated polyol assisted formaldehyde reduction method and (iii) subsequently used as the electrocatalyst for formic acid (FA) and ethylene glycol (EG) electro-oxidation. The structural and morphological properties of the electrocatalysts were studied using advanced physicochemical characterization techniques. The obtained results well evidence the homogeneous dispersion of Pt-Pd NPs on the surface of the carbon. Especially, $Pt_{0.5}Pd_1$/C exhibited excellent electrocatalytic property towards formic acid electro-oxidation reaction (FAOR) with a higher current density (256 mA cm^{-2}) and stability due to "third body effect". On the other hand, $Pt_1Pd_{0.5}$/C expressed superior electrochemical performance towards ethylene glycol electro-oxidation reaction (EGOR) due to the strong interaction between high Pt content and Pd. Hence, this work reveals the improved electrocatalytic performance of bi-metallic Pt-Pd NPs supported biomass-derived carbon as a promising anodic electrocatalyst towards FAOR and EGOR.

1. Introduction

Carbon materials derived from *agro-waste* have provoked significant interests as a catalyst support in various electrochemical conversion reactions [1]. Biomass is considered as one of the sustainable energy resource having exclusive features including, abundance, low cost, easily accessible, eco-friendly, and recyclable to sequester carbon-based materials. Excitingly, carbon materials derived from biomass possess higher specific surface area, organic oxygen functionalities, inborn hetero-atoms and tunable surface properties [2]. Especially, the presence of heteroatoms (N, S, P and B)

* Corresponding author.
E-mail address: selvankram@bu.edu.in (R. Kalai Selvan).

https://doi.org/10.1016/j.jcis.2019.10.121
0021-9797/

greatly influences the electronic and crystalline structures of the carbon materials which substantially improve the chemical stability, electrical conductivity, and electron-donor features [3]. Amongst, the carbon materials inherited with nitrogen species either as pyrrolic, pyridinic, or quaternary N groups provide wettability, more active sites, and homogeneous dispersion of metal nanoparticles with strong interaction [3]. Therefore, the nitrogen inherited carbon materials are widely employed as a catalyst support in various electrochemical anodic oxidation reactions especially in polymer exchange membrane fuel cells (PEMFCs) [4].

In PEMFCs, the selection of noble metal (catalyst) and its carbonaceous support (catalyst support) is an essential key component to facilitate anodic oxidation reaction for achieving 100% efficiency. Especially, the catalyst support should be highly efficient, evergreen, low cost, and electrochemically stable [4]. In this regard, various carbonaceous materials including carbon black, carbon nanotubes (CNTs), carbon nanofibers (CNFs), activated carbons (ACs), carbon aerogels (CAGs), reduced graphene oxides (rGO) have been reported as a promising support material [1,5]. Among these, biomass-derived carbon received many interests as catalyst support for loading metal catalysts, Pt, Pd, Ru, Sn, Ag, Ir, Au, etc. since it provides large active surface area for the homogeneous distribution which in turn improves the overall electrochemical performances [6]. Recently, various authors have been reported on the biomass-derived carbon with noble metals for various oxidation reactions including Pt dendrites supported soybean-derived-carbon for methanol oxidation [7], Pt nanowires loaded pectin derived porous carbon spheres for both methanol and ethanol electro-oxidation [8], Pt supported Okara-derived carbon (ODC) for methanol electro-oxidation [9], heteroatom loaded cotton waste-derived carbon for hydrazine oxidation [10], Pt NPs decorated carbon from *Artocarpus heterophyllus* seeds (AHS) for methanol oxidation reaction [11], Pt NP supported seafood waste-derived carbon for formic acid reaction [12], Pd supported activated carbon (Pd-AC800) for formic acid reaction [13] and Pd nanoparticles supported riboflavin (Pd/R-C) for ethylene glycol oxidation reaction [14]. Other than biomass-derived carbon, some interesting works have been reported on graphene decorated Pd [15] and PdCu clusters [16], and twisted PdCu nano chains on XC-72 carbon [17] as anodic catalyst for formic acid oxidation.

It is well known that methanol, ethanol, glycerol, formic acid, ethylene glycol, isopropanol have been used as the input fuels for PEMFCs since they considered as the green-fuels [5]. However, organic fuels like formic acid (FA) and ethylene glycol (EG) received significant interests in recent times. The FA delivers high open circuit potential, superior oxidation kinetics, negligible fuel crossover issues and it is safe compared to methanol [18,19]. As well as the formic acid electrooxidation reaction (FAOR) occurs via a twofold mechanism, i.e., direct/ dehydrogenation (to carbon-dioxide) and indirect/ dehydration (CO formation followed by CO_2) pathway [18]. On the other hand, the low toxicity, fast electro-oxidation, lower EG crossover via Nafion membrane, environmentally benign and oxalate production as a product, leads to the pioneering research motivation towards ethylene glycol electro-oxidation reaction (EGOR) [20]. Therefore, the formic acid and ethylene glycol provides a new scenario in the ethnic designing of electrolyte for polymer exchange membrane fuel cells due to their peculiarity of low cost, abundance, chemically stable, eco-friendly, high calorific value, ease of storage, and purity [14].

In this regard, the present work is concentrated on the preparation of nitrogen inherited carbon spheres (CS) from *Artocarpus heterophyllous seeds* (AHS) derived starch by hydrothermal method. *Artocarpus heterophyllus seeds (AHS)* is an abundant *agro-waste* available in the southern parts of Asian countries. It is rich in electro-active components such as vitamins, minerals, phytonutrients, starch, electrolytes, fibre, fat and protein [11]. The hydrothermal carbonization (HTC) is adopted in the present work due to the flexibility for tuning surface-chemical properties including, surface area, organic functionalities (oxygen and nitrogen), chemical and mechanical stability and morphology [21]. Pertinently, this report initially starts with the sequestration of carbon spheres from AHS (agro-waste) starch through HTC method followed by, high-temperature carbonization. Finally, the obtained carbon material was decorated with bi-metallic Pt-Pd nanoparticles/nanoalloys (NPs) through ethylene glycol solvated polyol assisted formaldehyde reduction method, since these nanoalloys are distinctly different from the single metals which endow fascinating properties in the conversion reactions [22]. The physical and morphological analysis revealed the turbostratic structure and spherical morphology of *N*-rich CS. As well as the surface chemical, structural and morphological characterizations of various compositions of Pt-Pd NPs decorated biomass-derived carbon also studied. Amongst, the $Pt_{0.5}Pd_1$/C and $Pt_1Pd_{0.5}$/C are identified as the best anodic electrocatalyst towards the oxidation reactions of formic acid and ethylene glycol, respectively.

2. Experimental methods and materials

2.1. Materials and reagents

Chloroplatinic acid (H_2PtCl_6), palladium (II) chloride ($PdCl_2$), sulphuric acid (H_2SO_4), Nafion ($C_7HF_{13}O_5S{\cdot}C_2F_4$) were purchased from Sigma-Aldrich. Sodium hydroxide (NaOH), hydrochloric acid (HCl), Ethanol (C_2H_5OH), formaldehyde (CH_2O), and Ethylene Glycol ($C_2H_6O_2$) were obtained from HiMedia Laboratories. All the purchased chemicals were used without further purification. All the solutions were prepared with double-distilled (D-D) water.

2.2. Preparation of hydrothermally derived carbon sphere

Initially, the carbon spheres (CS) were prepared from *agro-waste* derived starch through hydrothermal carbonization followed by physical activation. The schematic representation of the preparation procedure is given in Fig. 1. Initially, 5 g of starch powder was dispersed in 40 Ml of D-D water through sonication (15 min). Then, the citric acid (15 mg) was added to the mixture to catalyse the reaction. Then, the mixture was sealed in a 50 ml Teflon lined autoclave to undergo the HTC at a constant temperature of 180 °C for 24 h. The autoclave was left unsealed for about 12 h until it reaches room temperature. After attaining room temperature, the hydrochar was washed thoroughly with D-D water and ethanol several times and finally left to dry for 12 h at 100 °C. Followed by, the preparation of activated carbon was carried out by physical activation of hydrochar in a tubular furnace at a high temperature of 700 °C for 3 h under N_2 atmosphere. The obtained black carbon powder was crushed with glass mortar and sealed in an airtight container.

2.3. Preparation of bi-metallic Pt-Pd NPs decorated carbon spheres by polyol method

A conventional polyol reflux method was adopted to prepare electrocatalysts through ethylene glycol solvated formaldehyde reduction method. Typically, 50 mg of carbon is dispersed in D-D water/EG (1:2) through sonication for 30 min. Subsequently, different compositions of 12 mM of H_2PtCl_6 and 10 mM of $PdCl_2$ was dissolved separately in 10 ml of D-D water under sonication for 15 min. The desired amount of H_2PtCl_6 and $PdCl_2$ was added drop by drop into the carbon dispersion under vigorous stirring for 30 min. The percentage of carbon and noble catalyst loading was adjusted to produce 80:20 wt%, respectively. Then, 0.1 M NaOH

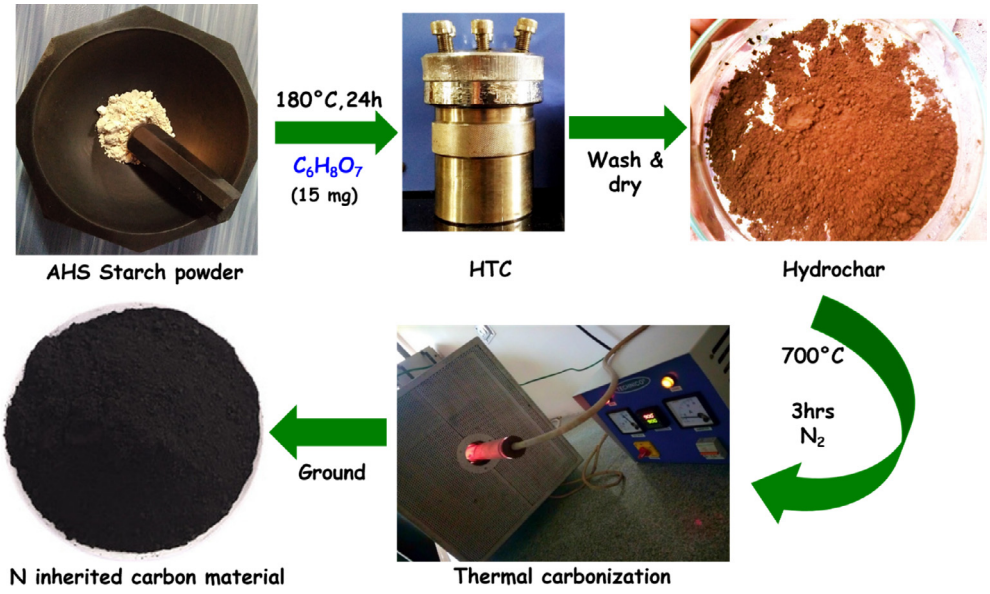

Fig. 1. Preparation scheme for the sequestration of CS from AHS starch powder.

was poured into the solution to adjust the pH 14, as it is essential to control the pH at each step before polyol reflux process. The resultant suspension was allowed to stir for 2 h at room temperature, followed by polyol reflux process at 120 °C for 3 h. The suspension was left to reach room temperature, and 0.1 M HCl was added dropwise into the cooled suspension to adjust pH 3. Later, the nanoparticles suspension was washed several times with D-D water and ethanol until it reaches pH 7. The thoroughly washed suspension is dried under vacuum at 80 °C for 12 h and ground homogeneously to obtain a fine powder (Fig. 2).

2.4. Structural characterizations

The as-prepared samples were characterized including advance Powder X-ray diffractometer (Cu-Kα1 radiation; λ = 1.5406 Å) for understanding the phase and crystal structure of the carbon and electrocatalyst materials, FT-IR analysis (Nicolet Impact 400 FT-IR spectrophotometer using KBr pellets) for identifying functional groups on the surface of carbon material. The graphitization degree and structural composition of the electrocatalysts were declared using Raman (WITech CRM200 confocal microscopy Raman system with a 488 NM laser) and X-ray photoelectron spectroscopy (Omicron Nanotechnology, Germany). The morphology of the electrocatalysts was analysed using Transmission Electron Microscopy and high-resolution transmission electron microscopy (JEOL JEM-2010, Japan).

2.5. Electrochemical characterizations

Electrochemical measurements were performed on a Bio-Logic SP150 work station using a standard three-electrode system. A GCE (3.0 mm, 0.071 cm^2) electrode polished with Al_2O_3 powder (0.05 μm) was used as the working electrode, the platinum wire was used as the counter electrode, and Ag/AgCl was used as the reference electrode. The electrocatalyst ink was prepared by dispersing 1 mg of the prepared electrocatalyst in 150 μL of Millipore water, 50 μL of isopropyl alcohol and 8 μL of Nafion through bath sonication for 15 min. Then, 2 μL of the electrocatalyst ink is drop-casted onto the finely polished GCE and dried in vacuum for 10 min before performing electrochemical measurements.

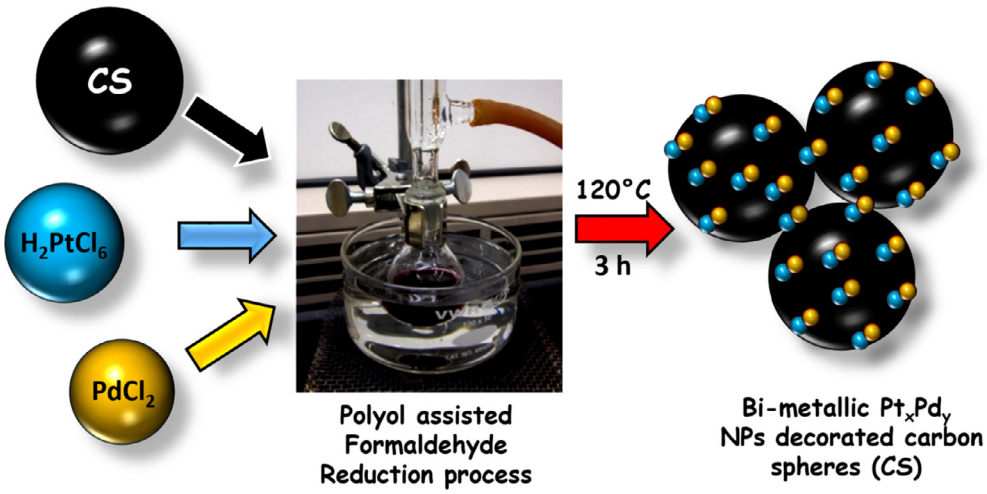

Fig. 2. Schematic representation for the preparation of bi-metallic Pt_xPd_y decorated on CS.

Cyclic Voltammetry (CV) was accomplished between −0.2 to 1.2 V (vs. Ag/AgCl) in 0.5 M H_2SO_4 electrolyte with or without 0.5 M formic acid (FA) and 0.5 M ethylene glycol (EG) solutions for FAOR and EGOR at room temperature, respectively. Also, the Chronoamperometric (CA) measurements were carried out in 0.5 M H_2SO_4 containing 0.5 M FA or 0.5 M EG solutions for the 1500 s. Electrochemical impedance spectroscopy (EIS) was performed in 0.5 M H_2SO_4 at a frequency range of 100 kHz to 1 Hz.

3. Results and discussion

3.1. Structural and morphological properties of hydrothermally derived carbon spheres

The structural (XRD, FTIR and Raman spectrum) properties of the hydrothermally derived carbon spheres (CS) are shown in Fig. 3. The obtained XRD pattern (Fig. 3a) exhibits two broad peaks at 2θ = 20-30° and 44.5°, corresponding to d_{002} - carbon interlayer-stacking and d_{100} - interlayer reflection of the hexagonal carbon planes. The observation confirms the formation of amorphous and sp^2 hybridized graphitic (i.e. turbostratic structure) carbon. Moreover, the ratio of the height of d_{002} peak determines as the empirical parameter (R) of CS, which is equal to 1.5, reveals the higher degree of the graphitization, due to a huge concentration of the parallel single layers or randomly distributed graphene sheets in the structure of carbon [23].

The FTIR spectrum (Fig. 3b) of CS displays the bands at 3400 cm^{-1} (hydroxyl groups), 2922 cm^{-1} (methyl and methylene groups), with two shoulder bands at 1706 cm^{-1} and 1620 cm^{-1} representing the stretching vibrations of carboxylic (C═O) and aromatic (C—C) compounds. The band at 1382 cm^{-1} corresponds to the aromatic CH and carboxyl carbonate compounds. The fingerprint band visible at 780 cm^{-1} due to benzene derivatives corresponding to C—H out-of-plane bending. Figure 3c represents the Raman spectra of CS obtained from AHS starch as a result of HTC. Here, two characteristic peaks are observed at 1351 cm^{-1} and 1590 cm^{-1}, corresponds to D and G band, respectively. The existence of D band is due to the formation of defects, vacancy and amorphous nature of CS, whereas the G band aroused due to the spitting mode of E_2g stretching of graphitic CS [24]. Therefore, Raman spectrum divulges the defective and graphitic nature, as well the ratio of two peaks (I_D/ I_G) reveals the graphitization degree (0.84) of the CS in concord with the XRD results (Fig. 3a).

The morphology and size of the CS were revealed through FE-SEM analysis at different magnifications (Fig. 4a–c) and size distribution histogram (Fig. 4d). It is observed from the FE-SEM image, the carbon material exhibited a 3D smooth sphere-like morphology with a homogeneous dispersion, as a result of the citric acid catalyst during HTC. According to Deshmukh et al., the carbon precursor gets transformed into carbon, and oxygen-containing functionalities, and finally gets transformed into CS (in concord with FTIR results). The mean diameter of the 3D smooth CS calculated from size distribution histogram image (Fig. 4d), is 4.71 μm, which reveals the existence of curling graphitic flakes with unbroken carbon layers containing dangling bonds of oxygen functionalities at the edges [25,26]. Overall, the citric acid assisted low-temperature HTC of AHS starch yielded, carbonaceous spheres with turbostratic structure, and high graphiticity, organized with numerous organic functionalities on its surface.

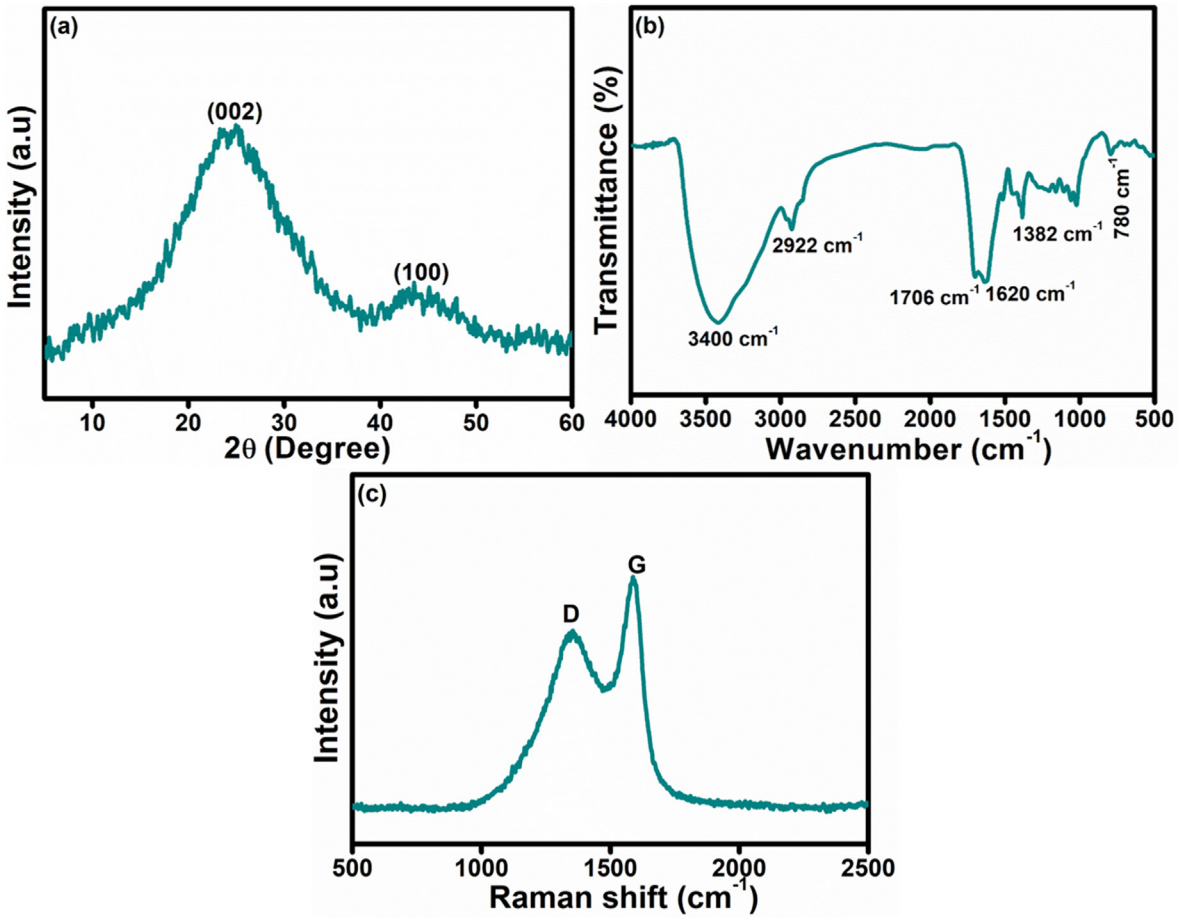

Fig. 3. (a) XRD pattern, (b) FTIR spectrum, and (c) Raman spectrum of CS.

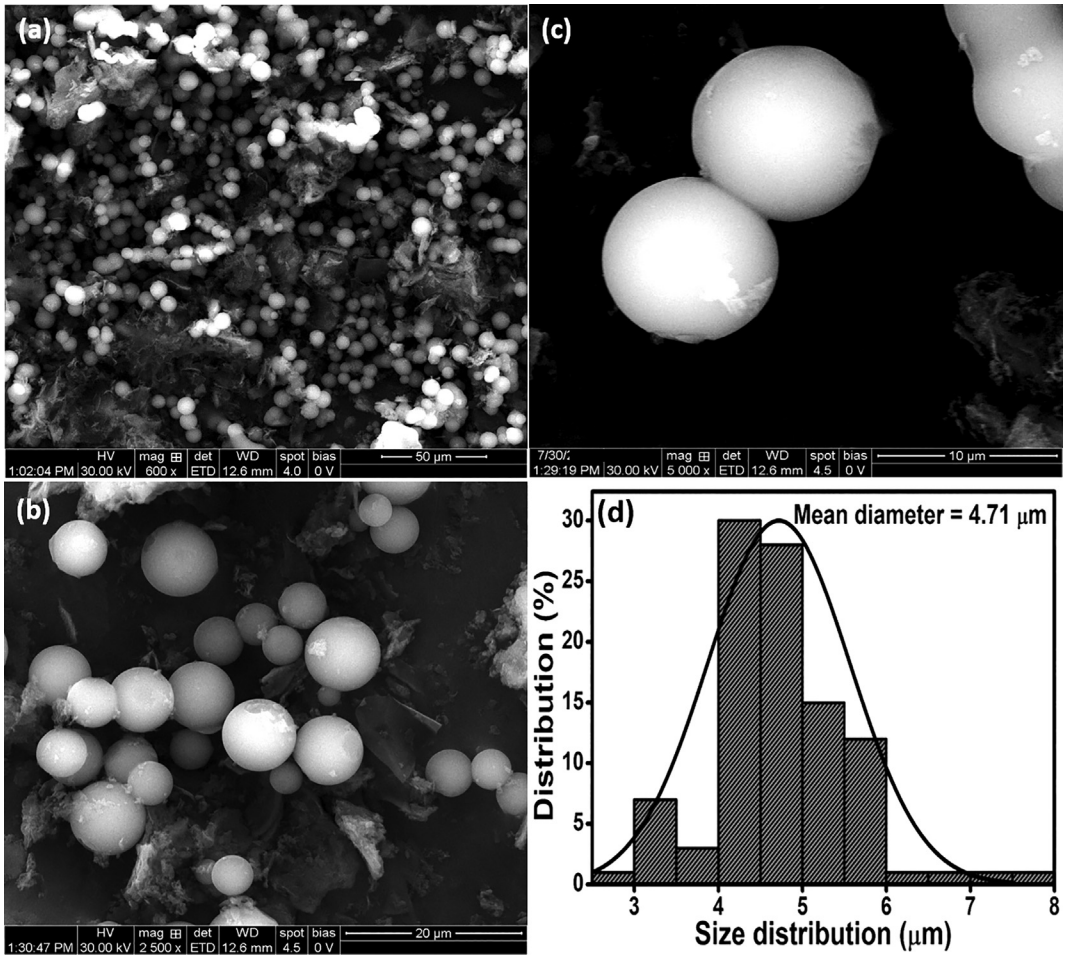

Fig. 4. (a–c) FE-SEM images and (d) particle size histogram of CS.

3.2. Structural and morphological properties of Pt-Pd decorated carbon spheres.

The XRD pattern of Pt_xPd_y/C is represented in Fig. 5. It is observed that all the electrocatalysts exhibit a broad peak at 20–30° corresponding to (0 0 2) plane, which is the characteristic peak of turbostratic carbon spheres [26]. In addition, the representative peaks at 39.8°, 46.1, 67.4, 81.3 and 85.6° corresponding to the planes of (1 1 1), (2 0 0), (2 2 0), (3 1 1) and (2 2 2), respectively, defines the face centred cubic (FCC) crystalline structure of Pt (JCPDS – 70-2431). Besides, the XRD peaks of Pt_xPd_y/C show a slight line shift towards higher angle (2θ) compared to Pt/C with well-defined characteristic peaks of FCC at 40.01, 46.5, 67.8, 81.7 and 56.1°. This is due to the substitution effect of Pd (JCPDS – 88-2335) nanoparticles (NPs) along with Pt NPs, which confirms the formation of bi-metallic Pt_xPd_y NPs on carbon spheres. The lattice parameter and crystallite size of Pt/C, Pd/C, Pt_1Pd_1/C, $Pt_{0.5}Pd_1$/C and $Pt_1Pd_{0.5}$/C are given in Table 1, which are comparative with the values of pure Pt (0.3923 nm) and Pd (0.3891 nm) FCC structure. Also, the crystallite size of the electrocatalysts was calculated using Scherrer's formula,

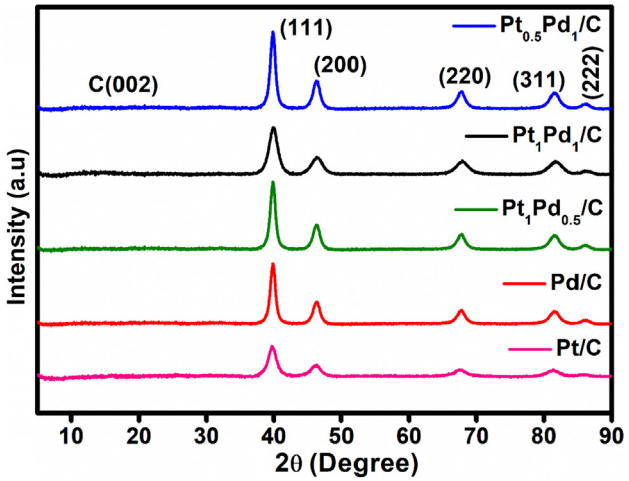

Fig. 5. XRD pattern of Pt_xPd_y/C electrocatalysts.

$$C_d = \frac{0.9\lambda}{\beta_{1/2} Cos\theta} \quad (1)$$

where, λ is the wavelength (1.54 Å), $\beta_{1/2}$ is the Full-Width Half Maximum (FWHM), *Cos*θ is the Bragg's angle.

From Table 1, it is clear that the crystallite size of Pt_xPd_y/C increases with the addition of Pd NPs, which reveals the influence of the addition of second metal in the composition of Pt/C. Further, the dispersion ratio (D_R) of Pt_xPd_y/C is calculated by van der Klink JJ equation (Eqs. (2)–(4)) [27],

$$N_S = 10L^2 - 20L + 12 \quad (2)$$

$$N_T = \frac{2\pi}{3}\left(\frac{C_d}{a}\right)^3 \quad (3)$$

Table 1
The structural parameters of Pt_xPd_y/C calculated from XRD.

Composition	Crystallite size (C_d), (nm)	Lattice parameter (a), (nm)	d- spacing of (1 1 1) plane, (nm)	$D_R = N_S/N_T$ %
Pt/C	2.95	0.3912	0.2271	50
Pd/C	4.60	0.3880	0.2256	49
Pt_1Pd_1/C	4.63	0.3902	0.2257	48
$Pt_1Pd_{0.5}/C$	4.01	0.3914	0.2250	56
$Pt_{0.5}Pd_1/C$	4.43	0.3896	0.2264	57

$$N_T = \left(\frac{10}{3}\right)L^3 - 5L^2 + \left(\frac{11}{3}\right)L - 1 \quad (4)$$

where, N_T and N_S are the total numbers of atoms and surface atoms per unit weight of the electrocatalyst respectively, L is the total number of layers (=d/I_d), a is the lattice parameter, and C_d is the crystallite size of the electrocatalyst. According to Bergeret, G. et al., the N_s is usually lying between 0 and 100% [26]. The calculated metal dispersion ratio is in the order of 57% ($Pt_{0.5}Pd_1/C$) > 56% ($Pt_1Pd_{0.5}/C$) > 50% (Pt/C) > 49% (Pd/C) > 48% (Pt_1Pd_1/C). Here, the $Pt_{0.5}Pd_1/C$ and $Pt_1Pd_{0.5}/C$ have higher metal dispersion ratio, which infers that a higher amount of bimetallic Pt_xPd_y NPs being decorated on the carbon surface [27,28].

Further, the elemental composition of Pt_xPd_y/C was studied using XPS spectra (Fig. 6). Fig. 6a, shows the survey spectra of Pt_x-Pd_y/C, confirming the presence of carbon (C), oxygen (O), nitrogen (N), Platinum nanoparticles (Pt NPs) and Palladium nanoparticles (Pd NPs). Fig. 6(b–d) shows the deconvoluted peaks of C1s, O1s and N1s, for $Pt_{0.5}Pd_1/C$, respectively. The C1s peak (Fig. 6b) exhibits the binding energies at 284.6, 286.3 and 288.0 eV corresponding to sp^2 bonded carbon C═C, C—O and O—C═O, respectively. The deconvoluted peaks of O1s peak (Fig. 6c) corresponding to 530.6, 532.9 and 533.4 eV are ascribed to O═C, C—OH and O—C, respectively. The excess presence of carboxyl and oxygen functionalities present on the surface of the carbon matrix is due to the phenolic compounds present in the *agro-waste*. The high-resolution N1s peak (Fig. 6d) observed at 400 eV reveals the inheritance of pyrrolic-N in the carbon material. This is due to, high-temperature carbonization effect, where the polysaccharides present in the precursor experiences bond breaking to form pyrrolic-N heterocycles through cross-linking mechanism [28]. Collectively, the organic and nitrogen functionalities provide large active sites for the noble metal to anchor on the carbon surface. Also, it helps in protonation, fast electron transfer and delivers wettability for the electrodes in fuel cell applications.

The XPS spectra (Fig. 7) shows the high-resolution deconvoluted peaks of Pt and Pd NPs for bimetallic $Pt_{0.5}Pd_1/C$ and $Pt_1Pd_{0.5}/C$. Also, the XPS high-resolution deconvoluted spectra of Pt and Pd NPs for bimetallic Pt/C, Pd/C and Pt_1Pd_1/C are shown in Fig. S1(a-d), respectively. The atomic weight percentage and binding energies from the XPS spectra of Pt_xPd_y/C are given in Table 2 and 3. It is clearly understood from Table 2, that, the atomic weight

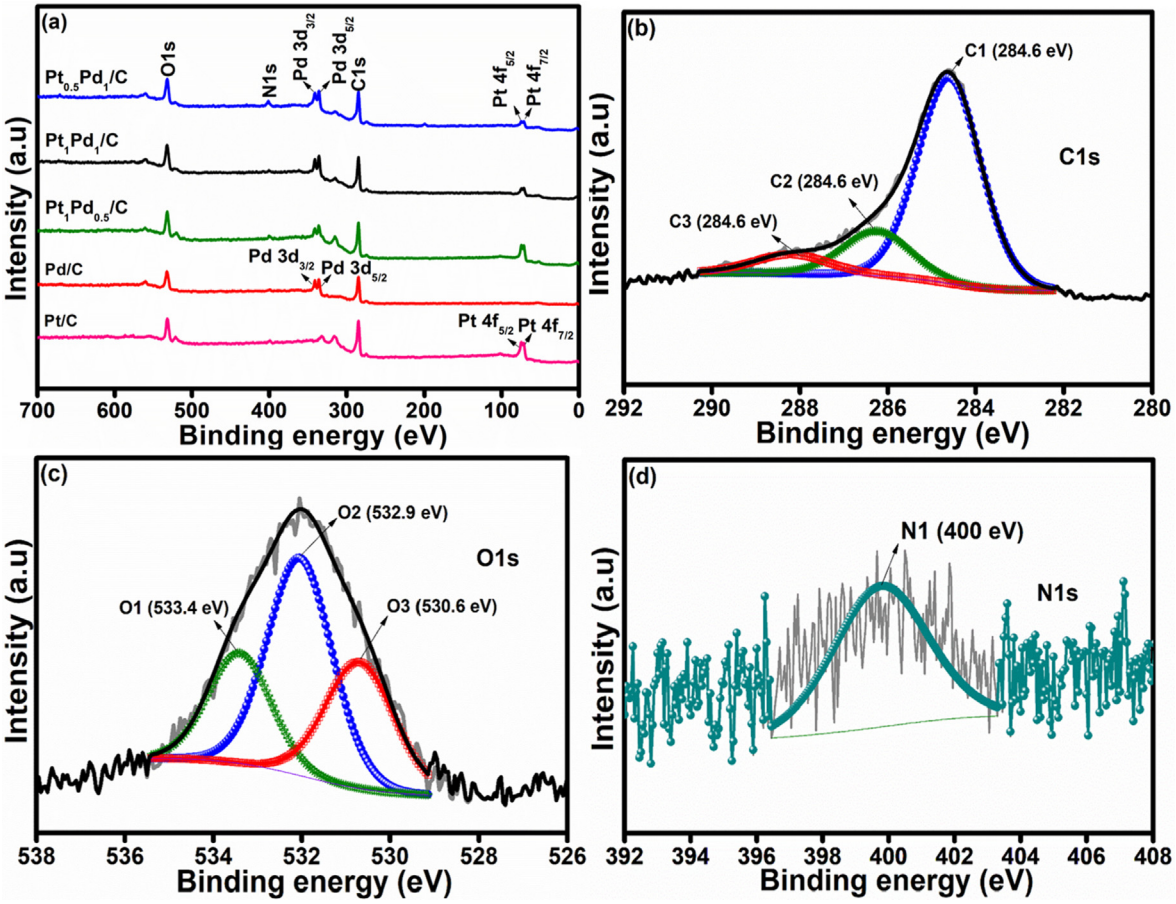

Fig. 6. (a) XPS survey spectra of Pt_xPd_y/C electrocatalysts, the deconvoluted spectrum of b) C1s, (c) O1s, and (d) N1s of $Pt_{0.5}Pd_1/C$.

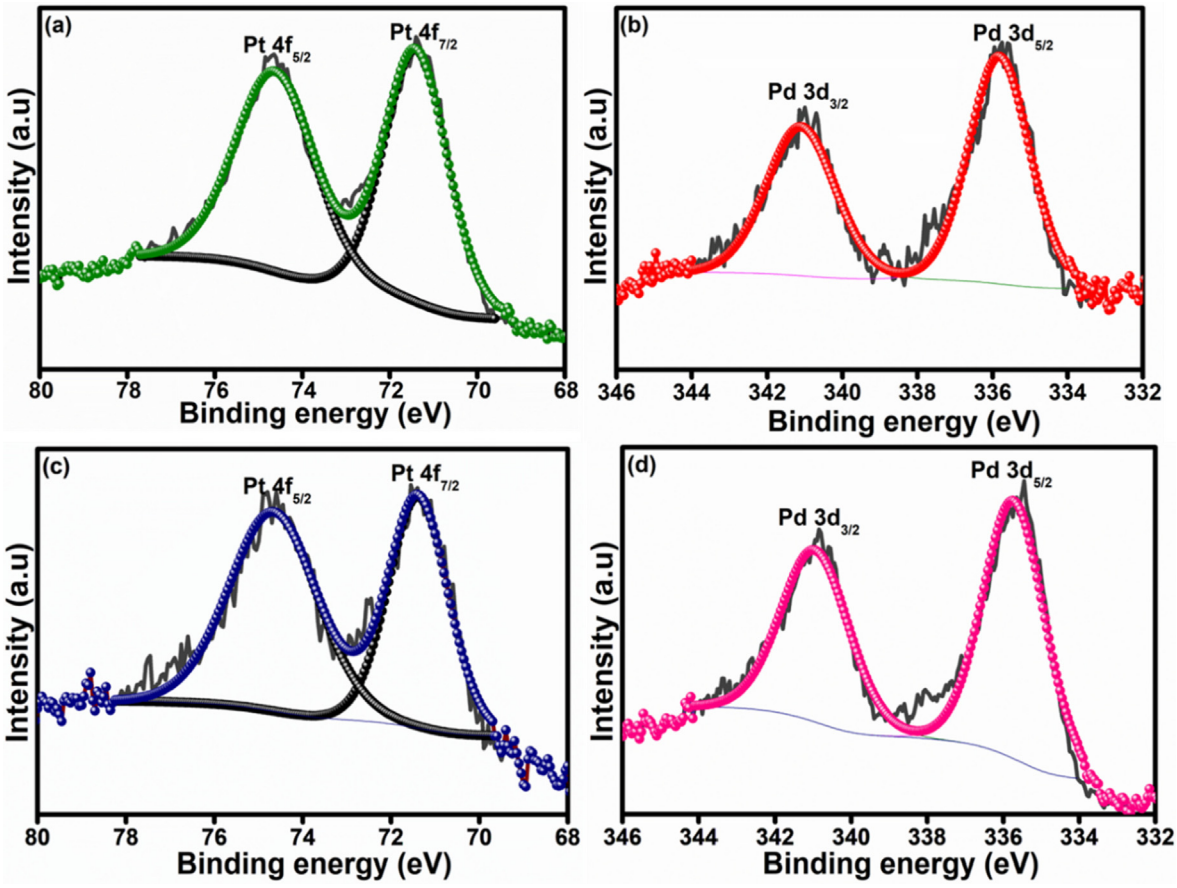

Fig. 7. XPS deconvoluted spectra of Pt and Pd in (a and b) $Pt_{0.5}Pd_1/C$; (and d) $Pt_1Pd_{0.5}/C$.

Table 2
Atomic weight percentage of Pt_xPd_y/C obtained from XPS spectral analysis.

Name	C1s %	O1s %	N1s %	Pt $4f_{7/2}$%	Pt $4f_{5/2}$%	Pd $3d_{3/2}$%	Pd $3d_{5/2}$%
Pt/C	78.4	18.1	2.1	0.9	0.3	–	–
Pd/C	72.1	19.1	2.1	–	–	2.8	2.7
$Pt_1Pd_{0.5}/C$	73.7	19.1	2.1	1.1	0.9	1.3	1.5
Pt_1Pd_1/C	72.3	19.5	2.1	0.6	0.4	2.7	2.4
$Pt_{0.5}Pd_1/C$	73.6	19.9	2.1	0.3	0.3	2.1	2.4

Table 3
Binding energies of Pt_xPd_y/C obtained from XPS spectral analysis.

Name	Pt $4f_{5/2}$ (eV)	Pt $4f_{7/2}$ (eV)	Pd $3d_{3/2}$ (eV)	Pd $3d_{5/2}$ (eV)
Pt/C	74.7	71.5	–	–
Pd/C	–	–	341.0	335.5
$Pt_1Pd_{0.5}/C$	74.6	71.4	340.9	335.8
Pt_1Pd_1/C	74.6	71.4	341.8	335.6
$Pt_{0.5}Pd_1/C$	74.6	71.4	340.4	335.2

percentage of nitrogen is equally distributed in all the electrocatalyst. Also, the difference in composition of Pt-Pd on carbon is confirmed from the tabulation according to the distribution of atomic weight percentage. From the analysis, the doublet peaks of Pt (Fig. 7a and c) such as Pt $4f_{5/2}$ and Pt$4f_{7/2}$ observed at binding energies 74.6 eV and 71.4 eV, respectively infers the metallic property of Pt NPs. Similarly, the XPS spectra of Pd (Fig. 7b and d) deconvoluted into two peaks Pd $3d_{3/2}$ and Pd $3d_{5/2}$ at 340.4 eV and 335.8 eV reveals the existence of metallic Pd NPs, respectively (Table 3). Irrespectively, the XPS spectra of Pt_1Pd_1/C, (Fig. S1c and d) exhibits Pd $3d_{3/2}$ at the binding energy of 341.4 eV (Table 3) which is the characteristic peak of Pd (II) species, infers that Pd got converted into Pd oxide (Pd^{2+}), which tend to deteriorate the electrochemical performance of the catalysts. From the observation, it is clear that the binding energies of $Pt_{0.5}Pd_1/C$ and $Pt_1Pd_{0.5}/C$ electrocatalyst have strong interaction between Pt and Pd on the carbon surface. Further, the EDX (Fig. S2) and elemental mapping (Fig. S3 and S4) were accomplished to determine the distributions of each element in the $Pt_{0.5}Pd_1/C$ and $Pt_1Pd_{0.5}/C$ electrocatalysts. The strong peaks at ~2 keV and ~3 keV of EDX analysis confirmed the existence of Pt and Pd NPs on the carbon surface, respectively. Also, the atomic weight percentage of each element calculated from

EDX analysis is given in Table S1 and S2 for $Pt_{0.5}Pd_1$/C and $Pt_1Pd_{0.5}$/C electrocatalysts, respectively. While, the elemental mapping analysis of $Pt_{0.5}Pd_1$/C and $Pt_1Pd_{0.5}$/C shows the homogenous distribution of Pt and Pd NPs on carbon surface in addition to with the existence of elements like carbon, oxygen and nitrogen, in concord with the XPS results.

TEM and HRTEM were used to analyse the morphological features and also to calculate the particle size of the Pt, $Pt_{0.5}Pd_1$, and $Pt_1Pd_{0.5}$ nanoparticles. Fig. 8 (a-c) shows the representative TEM images of Pt/C, $Pt_{0.5}Pd_1$/C, and $Pt_1Pd_{0.5}$/C electrocatalysts. It can be seen that the metallic nanoparticles are homogeneously dispersed on the carbon surface due to ethylene glycol solvated polyol reflux method. However, the observed insignificant agglomeration is in concord with the high dispersion ratio of bimetallic nanoparticles as calculated from the XRD pattern. The average size of the particles is calculated from the particle size histogram (Fig. S5), which are 2.00, 2.86 and 2.27 nm for Pt, $Pt_{0.5}Pd_1$ and $Pt_1Pd_{0.5}$ catalysts, respectively. Fig. 8(d–f) shows the HRTEM images of Pt/C, $Pt_{0.5}Pd_1$/C and $Pt_1Pd_{0.5}$/C. It clearly exposes the amorphous nature of the carbon surface and the well-defined lattice fringes. The calculated d-spacings are 0.202, 0.237 and 0.248 nm corresponding to the Pt and Pd (1 1 1) diffraction planes of Pt, $Pt_{0.5}Pd_1$ and $Pt_1Pd_{0.5}$ NPs, respectively. Fig. 8(g–i), shows the corresponding SAED pattern of Pt/C, $Pt_{0.5}Pd_1$/C, and $Pt_1Pd_{0.5}$/C respectively. The observed well-defined diffraction rings correspond to the (1 1 1), (2 0 0), (2 2 0), (3 1 1) and (2 2 2) planes of Pt, $Pt_{0.5}Pd_1$ and $Pt_1Pd_{0.5}$, respectively with face-centred cubic (fcc) structure. The obtained result is strongly supported by the XRD pattern. The morphology and SAED pattern reveals that ethylene glycol solvated polyol reflux assisted formaldehyde reduction has proved to be a promising approach for the decoration of bimetallic Pt-Pd NPs on the carbon surface.

3.3. Electrocatalytic properties of various Pt_xPd_y/C electrocatalysts

(a) Electrochemical properties in 0.5 M H_2SO_4 electrolyte

Cyclic voltammetric measurements are performed in 0.5 M H_2SO_4 for all the of Pt_xPd_y/C electrocatalyst at a scan rate of 20 mV s^{-1} under the steady-state condition. The electrochemical measurements are normalized according to electrocatalyst loading on GCE. The cyclic voltammogram (Fig. 9) of all the electrocatalysts (Pt/C, Pd/C, $Pt_1Pd_{0.5}$/C, Pt_1Pd_1/C, and $Pt_{0.5}Pd_1$/C) exhibited the typical characteristic features of hydrogen adsorption/desorption (H_{ads}/H_{des}) in the potential range of $-0.2 < E < 0.05$ V vs Ag/AgCl (Eq. (5)). On the other hand, the formation of OH_{ads} occurs beyond > 0.05 V vs Ag/AgCl (Eq. (6)). Here, the H_{ads} and OH_{ads} refers to the deposited hydrogen and the adsorbed hydroxyl species on the surface of the electrocatalyst, respectively [18,19].

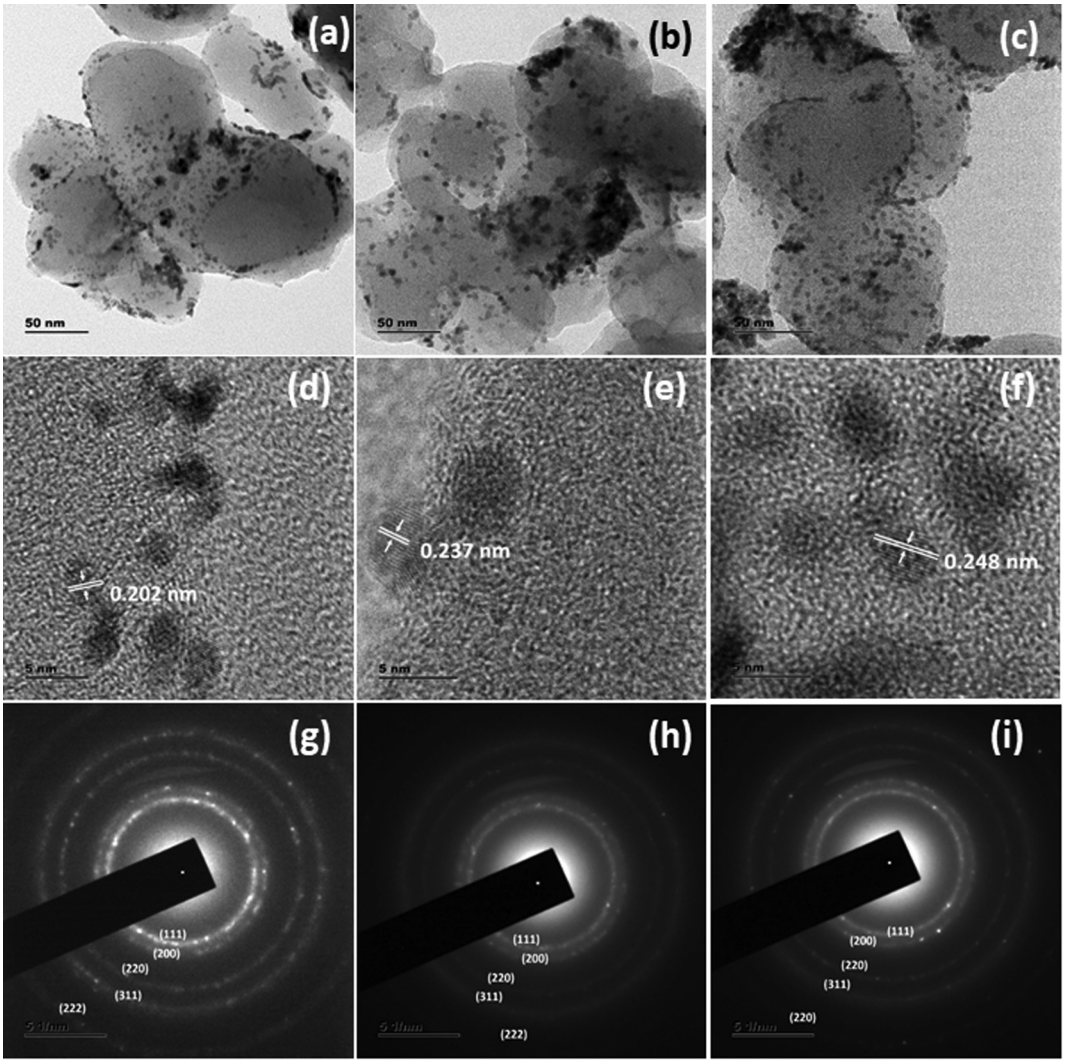

Fig. 8. (a–c) TEM images, (d–f) HRTEM images and (g–i) SAED pattern of Pt/C, $Pt_{0.5}Pd_1$/C, $Pt_1Pd_{0.5}$/C electrocatalyst.

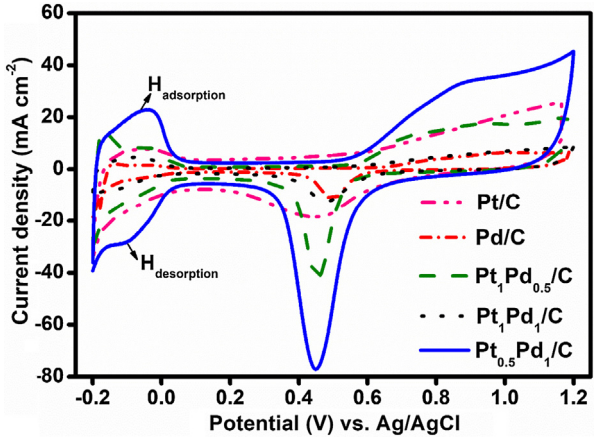

Fig. 9. The CV of various Pt_xPd_y/C electrocatalysts modified GCE in 0.5 M H_2SO_4 at a scan rate of 20 mV s^{-1}.

$$H_{ads} \leftrightarrow H^+ + e^- \quad (5)$$

$$2H_2O \rightarrow OH_{ads} + H_3O^+ + e^- \quad (6)$$

Interestingly, $Pt_1Pd_{0.5}$/C and $Pt_{0.5}Pd_1$/C exhibited more negative onset potential compared to the other electrocatalysts as given in Table 4. This is due to the bi-metallic nature of Pd with Pt, which provides oxygen-containing hydroxyl species (OH_{ads}) for the oxidation of intermediates under lower potential. Therefore, it enhances the electrocatalytic activity through direct electron transfer pathway [18]. Similarly, the observed cathodic peak around 0.4 V vs Ag/AgCl infers the reduction of Pd (II) oxide, which formed during the anodic reaction (at 0.6–1.0 V vs Ag/AgCl) on the surface of the electrocatalyst. Here, $Pt_1Pd_{0.5}$/C and $Pt_{0.5}Pd_1$/C exhibit a prominent cathodic peak compared to other catalysts due to its high electrolyte-electrode accessible surface area [19]. Further, the electrochemical surface area (ECSA) was calculated using equation (7) for all the catalysts and is given in Table 4.

$$ECSA = \frac{Q_H \times 10^2}{210 \times M_{Pt}} \quad (7)$$

Interestingly, the ECSA of $Pt_{0.5}Pd_1$/C (105.9 m^2g^{-1}) is high among the prepared catalysts as well as the reported PdRu nitrogen-containing super porous activated carbons (42.8 m^2g^{-1}) [29], Pt/Ni(OH)$_2$–NiOOH/Pd multi-walled hollow nanorod arrays (94.84 m^2g^{-1}) [30], Pt-Au/C (44.4 m^2g^{-1}) [31], Pd/ceria (93 $cm^2g^{-1}_{Pd}$) [32], Pd-Fe_2P/C (72.38 m^2g^{-1}) [33], PdAu-1.8 ($Pd_{36}Au_{64}$) (43.36 m^2g^{-1}) [34], Pt/Pd/ poly 1,5–diaminonaphthalene /GC (90.43 m^2g^{-1}) [35]. Similarly, the calculated mass activity (M_A) and surface activity (S_A) [11,30] of $Pt_{0.5}Pd_1$/C catalysts are high compared with other electrocatalysts (Table 4). This can be attributed to the smaller crystallite size, inherited nitrogen functionalities and homogeneous dispersion of $Pt_{0.5}Pd_1$ on the carbon support [36,37]. Here, the role of nitrogen functionalities inherited on the carbon surface has a predominant role for the electrocatalytic reactions in the following ways [38-42]. It provides abundant triple-phase boundary sites by means of facilitating large contact area between electrocatalyst and electrolyte [38], more space to accommodate any volumetric expansion [39], offering high surface sites for anchoring Pt nanoparticles [40], favourable conditions for adsorption of gas molecules [41], provides a large number of conductive pathways to achieve fast electrochemical reaction through diffusion and efficient mass transport in the active catalytic sites and carbon network [42].

Fig. 10 shows the Nyquist plots of Pt_xPd_y/C electrocatalyst measured in 0.5 M H_2SO_4 electrolyte in the frequency range from 100 kHz to 1 Hz. The obtained impedance parameters including solution resistance (Rs), charge transfer resistance (Rct), Warburg impedance (W) and constant phase element (CPE or Q) are given in Table 5. The measured charge transfer resistance (Rct) from the diameter of the semicircle are 0.163, 0.346, 0.732, 1.358, and 1.865 Ω corresponding to the catalyst in the favourable order of $Pt_{0.5}Pd_1$/C < $Pt_1Pd_{0.5}$/C < Pt/C < Pd/C < Pd_1Pt_1/C, respectively. As well as the observed straight line with an inclined slope (45°) infers the occurrence of mass transportation process through electroactive species diffusion [9]. Therefore, the prepared Pt_xPd_y/C electrocatalyst with low resistance will facilitate the electron transfer rate towards formic acid and ethylene glycol oxidation [13,14].

(b) Electrochemical properties in 0.5 M H_2SO_4 + 0.5 M CH_2O_2 electrolyte towards formic acid oxidation

Fig. 11a shows the cyclic voltammogram of the Pt_xPd_y/C electrocatalyst in 0.5 M H_2SO_4 + 0.5 M CH_2O_2 electrolyte at a scan rate of 20 mV s^{-1} for the formic acid oxidation and the calculated electrochemical parameters are given in Table 6. The observed prominent anodic peak of $Pt_{0.5}Pd_1$/C electrocatalyst at 0.16 V vs Ag/AgCl infers that the formic acid oxidation reaction occurs through a direct pathway and also the observed another slight fatter peak at 0.57 V vs Ag/AgCl reflects the contribution of the indirect pathway [19]. Interestingly, the same behaviour was observed for all the Pt_xPd_y/C electrocatalyst that elucidates the FA oxidation occurs

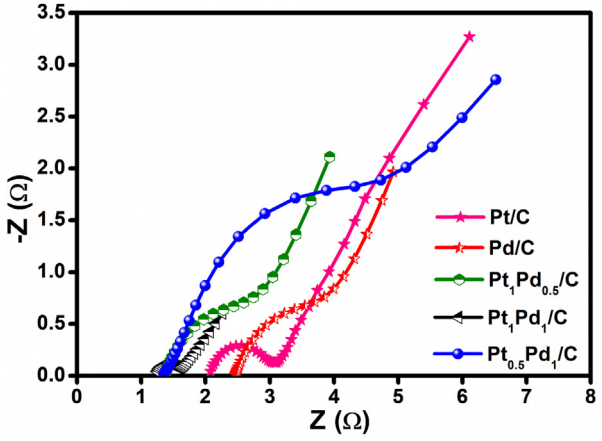

Fig. 10. Nyquist plots of various Pt_xPd_y/C electrocatalysts modified GCE in 0.5 M H_2SO_4.

Table 4
The electrochemical parameters calculated from the CV of $H_{ads/des}$ for different Pt_xPd_y/C electrocatalysts.

Sample	E_{oxi} (V)	E_{red} (V)	ECSA (m^2 g^{-1})	M_A (mA g^{-1})	S_{pt} (mA g^{-1})
Pt/C	0.62	0.46	68.4	3.58	5.8×10^{-1}
Pd/C	0.63	0.48	32.5	2.19	3.1×10^{-1}
$Pt_1Pd_{0.5}$/C	0.57	0.45	82.5	4.46	8.8×10^{-1}
Pt_1Pd_1/C	0.62	0.48	49.1	3.13	5.0×10^{-1}
$Pt_{0.5}Pd_1$/C	0.55	0.45	105.9	5.56	12.2×10^{-1}

Table 5
Parameters obtained from Nyquist plots of Pt_xPd_y/C electrocatalysts.

Catalysts	Rs (Ω)	Rct (Ω)	W
Pt/C	2.147	0.732	1.8
Pd/C	1.785	1.358	2.0
$Pt_1Pd_{0.5}$/C	1.503	0.346	6.3
Pd_1Pt_1/C	1.637	1.865	6.7
$Pt_{0.5}Pd_1$/C	1.344	0.163	5.5

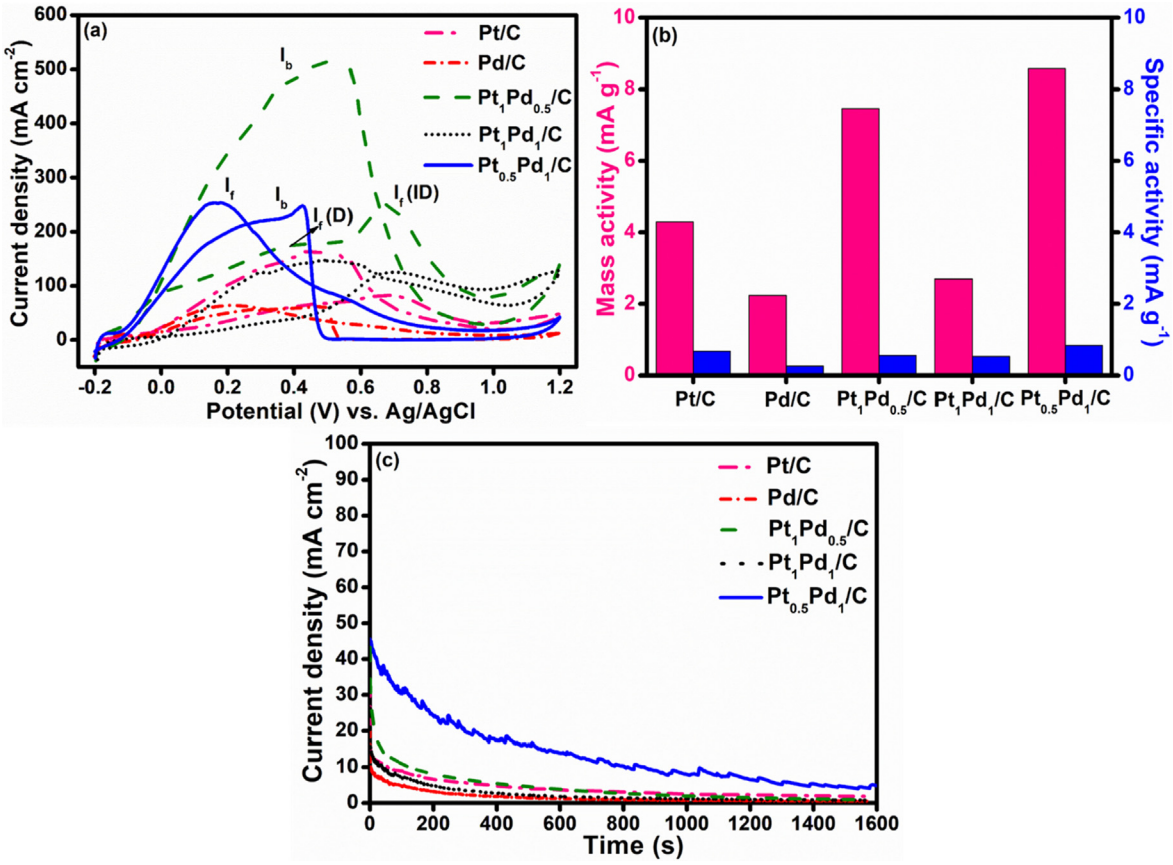

Fig. 11. (a) CV, (b) histogram of mass activity and specific activity and (c) CA of various Pt_xPd_y/C electrocatalyst modified GCE in 0.5 M H_2SO_4 + 0.5 M FA vs. Ag/AgCl.

Table 6
Electrochemical parameters calculated for Pt_xPd_y/C from CV towards FAOR.

Catalysts	E_{onset} (V)	E_{oxi} (V)		E_{red} (V)	I_f (mA cm^{-2})		I_f (D)/I_f (ID)	I_b (mA cm^{-2})	I_f (D)/I_b	ECSA (m^2 g^{-1})
		D	ID		D	ID				
Pt/C	−0.06	0.45	0.70	0.50	63	83	0.75	166	0.37	22.0
Pd/C	−0.15	0.2	0.65	0.47	61	27	2.27	62	0.92	10.4
$Pt_1Pd_{0.5}$/C	−0.18	0.42	0.67	0.53	211	286	0.73	458	0.67	24.7
Pd_1Pt_1/C	−0.01	0.32	0.66	0.54	34	125	0.27	149	0.22	12.8
$Pt_{0.5}Pd_1$/C	−0.12	0.16	0.56	0.42	256	72	3.55	250	1.02	32.9

through a dual-path mechanism [17]. In the direct (D) pathway, the FA is dehydrogenated directly into CO_2 without forming any poisonous intermediates (Eq. (8)). On the other hand, the CO_{ads} intermediates are generated (Eq. (9)) in the indirect (ID) pathway, which interacts with the OH_{ads} moieties (due to the formation of water dissociation according to Eq. (10)) and forms the CO_2 (Eq. (11)) [18].

$$M + CH_2O_2 \rightarrow I \rightarrow M + CO_2 + 2H^+ + 2e^- \quad (8)$$

$$M + CH_2O_2 \rightarrow M - CO_{ads} + H_2O \quad (9)$$

$$M + H_2O \rightarrow M - OH_{des} + H^+ + e^- \quad (10)$$

$$M - CO_{ads} + M - OH \rightarrow 2M + CO_2 + H^+ + e^- \quad (11)$$

where M is the metal active sites and I is the reactive intermediates. Unfortunately, the anodic peak potential of Pd/C (0.2 V vs Ag/AgCl) is high with the low current area when compared with $Pt_{0.5}Pd_1$/C catalyst. Therefore, it is clear that the catalyst, $Pt_{0.5}Pd_1$/C highly favours the electrochemical oxidation of formic acid compared to other catalysts.

Further, to understand the involvement of Pt_xPd_y/C and the tolerance of electrocatalyst towards CO poisoning during FAOR, the current intensity ratios such as I_f (D)/ I_f(ID) and I_f (D)/ I_b (backward current) were evaluated and given in Table 6. Among the prepared catalysts, $Pt_{0.5}Pd_1$/C has a higher value of I_f (D)/I_f (ID) and I_f (D)/I_b ratio. It infers that $Pt_{0.5}Pd_1$/C provides higher support towards direct oxidation of FA via dehydrogenation and its high tolerance against CO poisoning effect [19]. Though the FAOR proceeds via a dual-path mechanism, the intensity of direct forward current (256 mA cm^{-2}) is higher than the flatter indirect forward current (72 mA cm^{-2}), which infers that the diminishing effect of CO poisoning and the superior activity of $Pt_{0.5}Pd_1$/C. Similarly, the calculated mass activity and specific activity of $Pt_{0.5}Pd_1$/C (Fig. 11b) is also remarkable, expressing its high electrocatalytic suitability towards FAOR. Moreover, the durability test was conducted using the chronoamperometric technique for the Pt_xPd_y/C electrocatalyst in 0.5 M H_2SO_4 + 0.5 M FA (Fig. 11c). It is observed that $Pt_{0.5}Pd_1$/C exhibits quasi-steady-state stability over 500 s, starting with a higher initial current compared to the other catalysts. It is due to

the dehydrogenation [16,18] pathway undergone by the electrocatalyst during protonation and reached a steady, stable state beyond 750 s. Overall, the prepared bimetallic electrocatalyst $Pt_{0.5}$-Pd_1/C expressed a lower onset potential (E_{onset}) of −0.12 V vs Ag/AgCl compared to the other composite electrocatalysts including Pt NPs embedded with carbon matrix derived from seafood waste [12] and Pd NPs embedded with activated carbon obtained from lignosulfonate composite [13], revealing its superior catalytic activity. Further, the higher dispersion ratio and crystallite size (XRD and TEM) is also one of the major reasons for the facile protonation and thus obtained the enhanced electrochemical performance towards FAOR.

Fig. 12 shows the TEM and HRTEM images of $Pt_{0.5}Pd_1$/C electrocatalyst measured after the durability studies. It is observed that the Pt and Pd NPs still exist on the carbon surface homogeneously without any significant agglomeration. However, the HRTEM image explores the loss in crystalline of the Pt and Pd NPs with unclear fringes on the amorphous carbon surface. However, the SAED pattern exhibits only a few visible ring corresponding to (1 1 1) and (2 0 0) plane, in concord with the XRD results.

(c) Electrochemical properties in 0.5 M H_2SO_4 + 0.5 M $C_2H_6O_2$ towards ethylene glycol oxidation

Fig. 13a shows the CV of Pt_xPd_y/C NPs electrocatalyst in 0.5 M H_2SO_4 + 0.5 M EG electrolyte at a scan rate of 20 mV/s in the potential range of −0.2 to 1.2 V vs. Ag/AgCl. It shows that the electrochemical performance of the prepared electrocatalyst is irreversible with the formation of two oxidation mountain peaks similar to methanol oxidation reaction. Among the prepared catalysts, the $Pt_1Pd_{0.5}$/C exhibits a higher current density of 72.8 mA cm^{-2} (at 0.63 V vs Ag/AgCl) and 74.2 mA cm^{-2} (at 0.46 V vs Ag/AgCl), during forward and reverse scans, respectively. As well as, comparatively (Table 7) the onset potential of $Pt_1Pd_{0.5}$/C (0.21 V vs Ag/AgCl) is very less and the oxidation current density is higher during the reverse scan due to the oxidation of newly chemisorbed alcohol species. Moreover, the electrocatalyst exhibit superior mass and specific activity (Fig. 13 b) towards ethylene glycol oxidation. The obtained electrocatalytic performance of $Pt_1Pd_{0.5}$/C NPs is comparable with the reported Pd NPs decorated carbon–ceria composite supports [43] and the bimetallic PtPd alloyed nanoflowers on reduced graphene oxide (rGO-PtPd nanoflowers) [44].

It is well known that the EG oxidation involves the production of chemisorbed CO on the Pt surface during the oxidation reaction (Equation (12)). Hence, more number of active sites of Pt will be blocked by these poisoning species and thus hinders the adsorption of EG molecules further. Therefore, the overall electrochemical activity towards EG oxidation will be reduced. Interestingly, the addition of Pd NPs along with Pt NPs on the carbon surface by forming $Pt_1Pd_{0.5}$/C, enhances the electrochemical activity due to the third body effect [14], (Eqs. (13) and (14)),

$$Pt(CH_2O_{2ads}) \rightarrow Pt(CO_{ads}) + H_2O \quad (12)$$

$$Pd + H_2O \rightarrow Pd(OH)_{ads} + H^+ + e^- \quad (13)$$

$$Pd(OH)_{ads} + Pt(CO)_{ads} \rightarrow Pt + Pd + CO_2 + H^+ + e^- \quad (14)$$

From the above set of equations, it is clear that the enhanced catalytic activity is because of the formation of $Pd(OH)_{ads}$ species by the attraction of Pd NPs with H_2O molecules (Equation (13)).

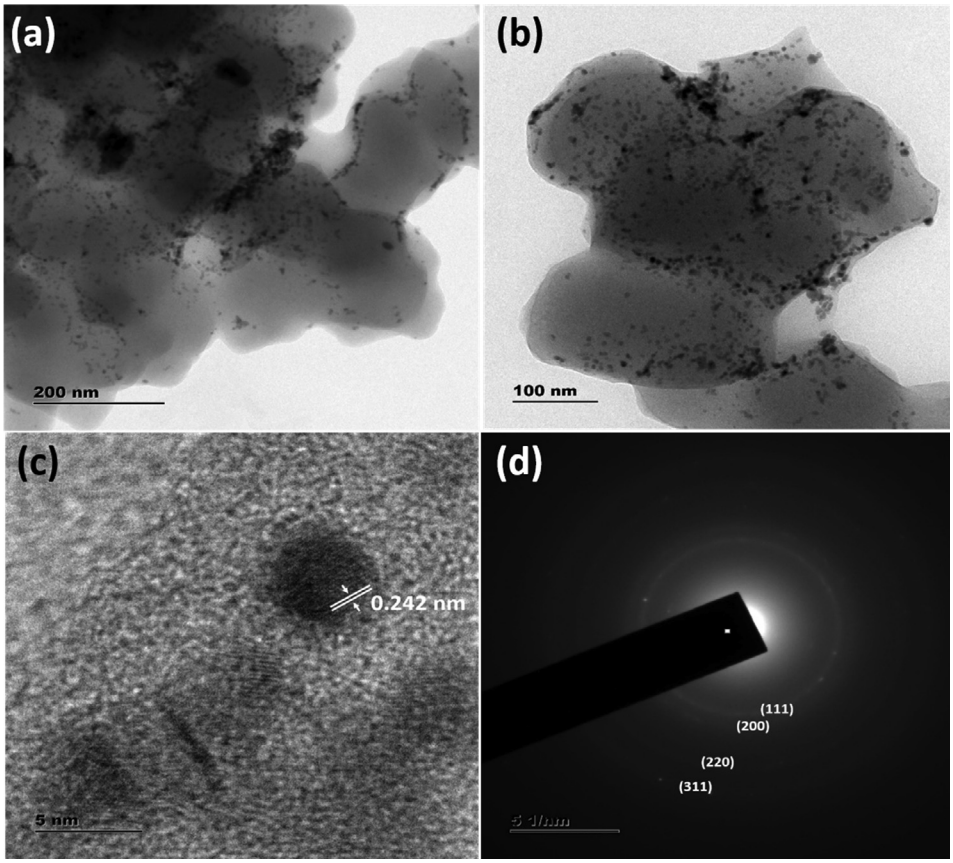

Fig. 12. (a and b) TEM, (c) HRTEM images and (d) SAED pattern of $Pt_{0.5}Pd_1$/C electrocatalyst after electrochemical stability test.

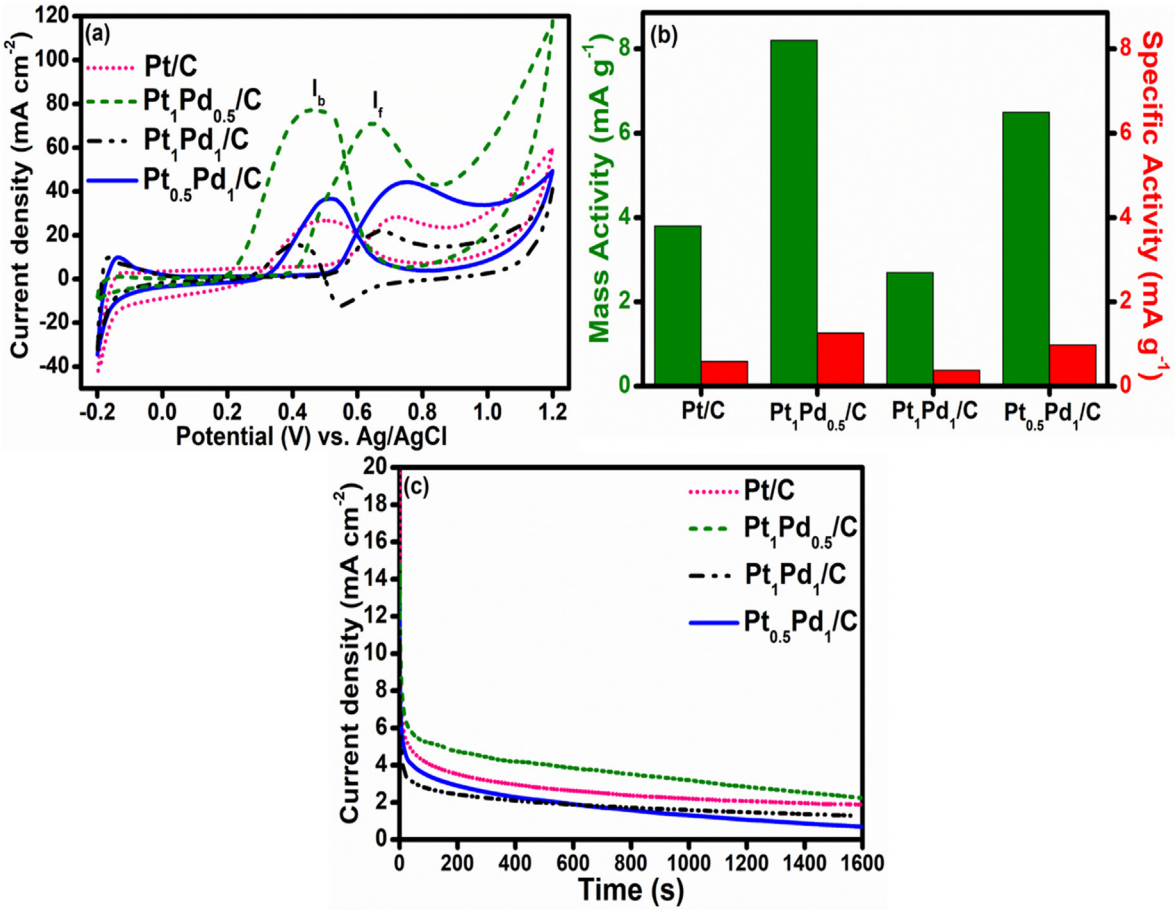

Fig. 13. (a) CV, (b) histogram of mass and specific activity and (c) CA of various Pt_xPd_y/C electrocatalyst modified GCE in 0.5 M H_2SO_4 + 0.5 M EG vs. Ag/AgCl.

Table 7
Electrochemical parameters calculated for Pt_xPd_y/C electrocatalysts from the CV towards EGOR.

Catalysts	E_{onset} (V)	E_{OXI} (V)	E_{RED} (V)	I_f (mA cm^{-2})	I_b (mA cm^{-2})	I_f/I_b	ECSA (m^2 g^{-1})
Pt/C	0.50	0.71	0.49	28.6	26.7	1.02	18.3
$Pt_1Pd_{0.5}$/C	0.21	0.63	0.46	73.8	74.2	0.99	31.8
Pd_1Pt_1/C	0.54	0.66	0.41	22.1	17.8	1.24	8.03
$Pt_{0.5}Pd_1$/C	0.51	0.73	0.51	44.3	36.9	1.20	2.71

Therefore, the Pd NPs on the catalyst surface helps to remove the CO species by oxidation from the surface of the electrocatalyst to produce CO_2. Moreover, The CA (Fig. 13c) was conducted on the Pt_xPd_y/C NPs electrocatalyst in 0.5 M H_2SO_4 + 0.5 M EG medium to measure its durability towards EGOR. It is observed that $Pt_1Pd_{0.5}$/C starts with a higher initial current compared to the other catalysts and exhibits slight quasi-steady-state stability over 250 s due to CO poisoning effect and reaches a steady, stable state up to 1600 s.

Fig. 14(a–c) shows the measured TEM and HRTEM images of $Pt_1Pd_{0.5}$/C electrocatalyst after the stability test. From the TEM observation, it is seen that the electrocatalysts remain unchanged in terms of morphology and the particle size. On the other hand, the HRTEM image shows the undistinguishable fringes, which corroborates the loss of crystallinity. Further, the SAED pattern (Fig. 14d) exhibits a d-spacing of 0.204 nm with the rings being visible with the diffraction along with the diffraction planes, which is in concord with the XRD and TEM analysis.

Overall, nitrogen inherited smooth carbon sphere is obtained from AHS starch, by HTC method followed by high-temperature carbonization. Then, the obtained CS was decorated homogeneously with Pt and Pd nanoparticles by ethylene glycol solvated polyol reflux assisted formaldehyde reduction process. The physical and chemical characterizations on the Pt_xPd_y/C were performed. Amongst, $Pt_{0.5}Pd_1$/C and $Pt_1Pd_{0.5}$/C exhibited higher dispersion ratio of 56 and 57, respectively, which clearly infers the homogeneous dispersion of the electrocatalyst on the CS surface. Further, the $Pt_{0.5}Pd_1$/C electrocatalyst demonstrated excellent electrocatalytic performance toward formic acid oxidation reaction with a high current density of 256 mA cm^{-2}, mass activity, specific activity and high stability. While, $Pt_1Pd_{0.5}$/C exhibited a remarkable electrocatalytic activity towards ethylene glycol oxidation reaction with a peak current density of 73.8 mA cm^{-2}, mass activity, specific activity and stability. Therefore, the synergetic catalyst with peculiar surface chemistry and electronic effect exhibited higher catalytic activity and stability towards FAOR and EGOR due to the third body ensemble effect.

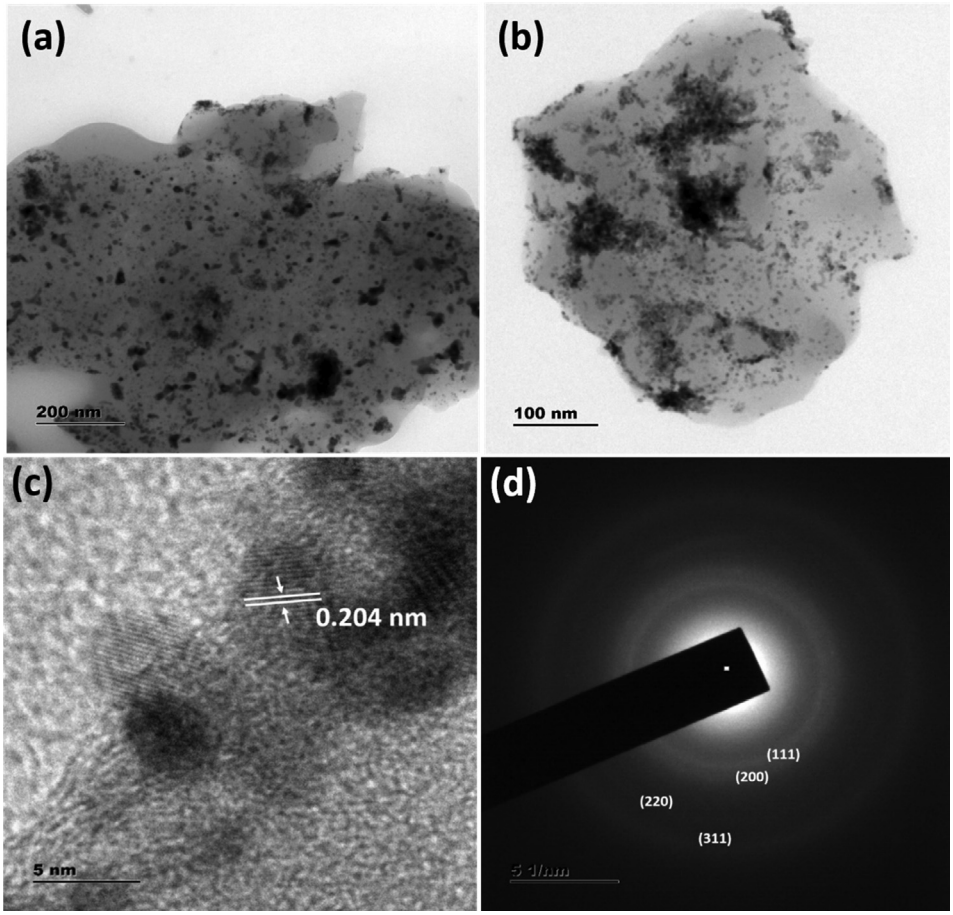

Fig. 14. (a & b) TEM, (c) HRTEM images, and (d) SAED pattern of $Pt_1Pd_{0.5}$/C electrocatalyst after electrochemical stability test.

4. Conclusion

This manuscript summarizes the preparation of nitrogen inherited smooth carbon spheres from *Artocarpus heterophyllus* seed starch through hydrothermal carbonization method and high-temperature carbonization. Followed by, the decoration of highly efficient bi-metallic Pt_xPd_y NPs on nitrogen inherited smooth carbon sphere through polyol assisted formaldehyde reduction method. The obtained bi-metallic Pt_xPd_y/C was characterized using physicochemical and morphological analysis. As a result, the Pt_xPd_y/C exhibited a typical face centred cubic structure with high crystallinity and dispersion ratio. The morphological analysis confirms the homogenous decoration of Pt and Pd NPs on the surface of nitrogen inherited smooth carbon spheres due to ethylene glycol solvated polyol assisted formaldehyde reduction, with a mean particle size of ~2 nm. The Pt_xPd_y/C was employed as an anodic electrocatalyst towards the formic acid and ethylene glycol electrooxidation in acidic media. Of the prepared electrocatalyst, the Pt_xPd_y/C containing large Pd NPs exhibited superior electrocatalytic activity towards FAOR, with high current density, mass, specific activity, and superior durability. Whereas, the composition rich with Pt NPs favours EGOR with ultra-high electrochemical activity compared to reported works. Therefore, this work is a pioneering report that expresses the interesting aspects of the preparation of electrocatalyst support material from *agro-waste* biomass energy resource for fuel cell oxidation reaction.

Acknowledgement

Prof. Yun Sung Lee greatly acknowledges the National Research Foundation of Korea (NRF) grant funded by the Korean government (Ministry of Science, ICT & Future Planning) (No. 2019R1A4A2001527).

Appendix A. Supplementary material

Supplementary data to this article can be found online at https://doi.org/10.1016/j.jcis.2019.10.121.

References

[1] H.O. Pierson, Handbook of carbon, graphite, diamonds and fullerenes: processing, properties and applications, William Andrew 1 (2012) 419. ISBN: 9786612002571.
[2] R.C. Bansal, M. Goyal, Activated carbon adsorption, CRC Press, 2005, pp. 1–520. ISBN 9781420028812.
[3] J. Deng, M. Li, Y. Wang, Biomass-derived carbon: synthesis and applications in energy storage and conversion, Green Chem. 18 (2016) 4824–4854.
[4] R. Rajagopalan, A. Balakrishnan, Innovations in engineered porous materials for energy generation and storage applications, CRC Press: Boca, Raton, FL, USA, 2018, p. 392.
[5] G.L. Soloveichik, Liquid fuel cells, Beilstein J. Nanotechnol. 5 (2014) 1399–1418.
[6] L. An, T. Zhao, Anion exchange membrane fuel cells: principles, materials and systems, Springer, 2018, pp. 1–346. ISBN: 9783319713717.

[7] T. Zhou, H. Wang, S. Ji, V. Linkov, R. Wang, Soybean-derived mesoporous carbon as an effective catalyst support for electrooxidation of methanol, J. Power Sour. 248 (2014) 427–433.
[8] Y. Fan, P.-F. Liu, Z.-J. Yang, T.-W. Jiang, K.-L. Yao, R. Han, X.-X. Huo, Y.-Y. Xiong, Bi-functional porous carbon spheres derived from pectin as electrode material for supercapacitors and support material for Pt nanowires towards electrocatalytic methanol and ethanol oxidation, Electrochim. Acta 163 (2015) 140–148.
[9] T. Zhou, H. Wang, S. Ji, H. Feng, R. Wang, Synthesis of mesoporous carbon from okara and application as electrocatalyst support, Fuel Cells 14 (2014) 296–302.
[10] T.L. Silva, A.L. Cazetta, T. Zhang, K. Koh, R. Silva, T. Asefa, V.C. Almeida, Nanoporous heteroatom-doped carbons derived from cotton waste: efficient hydrazine oxidation electrocatalysts, ACS Appl. Energy Mater. 2 (2019) 2313–2323.
[11] P. Rupa Kasturi, R. Kalai Selvan, Y.S. Lee, Pt decorated Artocarpus heterophyllus seed-derived carbon as an anode catalyst for DMFC application, RSC Adv. 6 (2016) 62680–62694.
[12] G.A. El-Nagar, M.A. Hassan, I. Lauermann, C. Roth, Efficient direct formic acid fuel cells (DFAFCs) anode derived from seafood waste: migration mechanism, Sci. Rep. 7 (2017) 17818.
[13] Y.-J. Jia, J.-C. Jiang, K. Sun, C. Chen, Oxidation of formic acid over palladium catalyst supported on activated carbon derived from polyaniline and modified lignosulfonate composite, J. Fuel Chem. Technol. 45 (2017) 100–105.
[14] W. Wang, W. Jing, Y. Liu, Y. Wang, J. Zhao, Z. Lei, Supporting Pd nanoparticles on riboflavin-derived carbon: an efficient electrocatalyst for ethylene glycol oxidation, Ionics 24 (2018) 1745–1754.
[15] L.Y. Zhang, Z.L. Zhao, C.M. Li, Formic acid-reduced ultrasmall Pd nanocrystals on graphene to provide superior electocatalytic activity and stability toward formic acid oxidation, Nano Energy 11 (2015) 71–77.
[16] Z. Zhang, Y. Gong, D. Wu, Z. Li, Q. Li, L. Zheng, W. Chen, W. Yuan, L.Y. Zhang, Facile fabrication of stable PdCu clusters uniformly decorated on graphene as an efficient electrocatalyst for formic acid oxidation, Int. J. Hydrogen Energy 44 (2019) 2731–2740.
[17] L.Y. Zhang, Y. Gong, D. Wu, G. Wu, B. Xu, L. Bi, W. Yuan, Z. Cui, Twisted palladium-copper nanochains toward efficient electrocatalytic oxidation of formic acid, J. Coll. Interf. Sci. 537 (2019) 366–374.
[18] Y. Gong, X. Liu, Y. Gong, D. Wu, B. Xu, L. Bi, L.Y. Zhang, X.S. Zhao, Synthesis of defect-rich palladium-tin alloy nanochain networks for formic acid oxidation, J. Coll. Interf. Sci. 530 (2018) 189–195.
[19] L.Y. Zhang, Y. Gong, D. Wu, Z. Li, Q. Li, L. Zheng, W. Chen, Palladium-cobalt nanodots anchored on graphene: In-situ synthesis, and application as an anode catalyst for direct formic acid fuel cells, Appl. Surf. Sci. 469 (2019) 305–311.
[20] A. Serov, C. Kwak, Recent achievements in direct ethylene glycol fuel cells (DEGFC), Appl. Catal. B 97 (2010) 1–12.
[21] T. Wang, Y. Zhai, Y. Zhu, C. Li, G. Zeng, A review of the hydrothermal carbonization of biomass waste for hydrochar formation: process conditions, fundamentals, and physicochemical properties, Renew. Sustain. Energy Rev. 90 (2018) 223–247.
[22] H. Fang, J. Yang, M. Wen, Q. Wu, Nanoalloy materials for chemical catalysis, Adv. Mater. 30 (2018) 1705698.
[23] S. Chen, K. Xing, J. Wen, M. Wen, Q. Wu, Y. Cui, Hierarchical assembly and superior sodium storage properties of a sea-sponge structured C/SnS@C nanocomposite, J. Mater. Chem. A 6 (2018) 7631–7638.
[24] T. Qiu, J.-G. Yang, X.-J. Bai, Y.-L. Wang, The preparation of synthetic graphite materials with hierarchical pores from lignite by one-step impregnation and their characterization as dye absorbents, RSC Adv. 9 (2019) 12737–12746.
[25] J. Bucher, J. Van der Klink, Electronic properties of small supported Pt particles: NMR study of Pt 195 hyperfine parameters, Physical Review B 38 (1988) 11038.
[26] G. Bergeret, P. Gallezot, Particle size and dispersion measurements, in: Handbook of Heterogeneous Catalysis: Online, 2008, pp. 738–765.
[27] X.-L. Xing, Y.-F. Zhao, H. Li, C.-T. Wang, Q.-X. Li, W.-B. Cai, High Performance Ag rich Pd-Ag bimetallic electrocatalyst for ethylene glycol oxidation in alkaline media, J. Electrochem. Soc. 165 (2018) J3259–J3265.
[28] L.-H. Zhang, W.-C. Li, H. Liu, Q.-G. Wang, L. Tang, Q.-T. Hu, W.-J. Xu, W.-H. Qiao, Z.-Y. Lu, A.-H. Lu, Thermoregulated phase-transition synthesis of two-dimensional carbon nanoplates rich in Sp_2 carbon and unimodal ultramicropores for kinetic gas separation, Angew. Chem. Int. Ed. 57 (2018) 1632–1635.
[29] H. Wang, Y. Li, C. Li, Z. Wang, Y. Xu, X. Li, H. Xue, L. Wang, Hyperbranched PdRu nanospine assemblies: an efficient electrocatalyst for formic acid oxidation, J. Mater. Chem. A 6 (2018) 17514–17518.
[30] H. Xu, L.-X. Ding, J.-X. Feng, G.-R. Li, Pt/Ni $(OH)_2$–NiOOH/Pd multi-walled hollow nanorod arrays as superior electrocatalysts for formic acid electrooxidation, Chem. Sci. 6 (2015) 6991–6998.
[31] H. Fan, M. Cheng, L. Wang, Y. Song, Y. Cui, R. Wang, Extraordinary electrocatalytic performance for formic acid oxidation by the synergistic effect of Pt and Au on carbon black, Nano Energy 48 (2018) 1–9.
[32] L. Ye, A.H. Mahadi, C. Saengruengrit, J. Qu, F. Xu, S.M. Fairclough, N. Young, P.-L. Ho, J. Shan, L. Nguyen, Ceria nanocrystals supporting Pd for formic acid electrocatalytic oxidation: prominent polar surface metal support interactions, ACS Catal. 9 (2019) 5171–5177.
[33] F. Wang, H. Xue, Z. Tian, W. Xing, L. Feng, Fe_2P as a novel efficient catalyst promoter in Pd/C system for formic acid electro-oxidation in fuel cells reaction, J. Power Sour. 375 (2018) 37–42.
[34] T. Szumełda, A. Drelinkiewicz, E. Lalik, R. Kosydar, D. Duraczyńska, J. Gurgul, Carbon-supported Pd_{100}-XAuX alloy nanoparticles for the electrocatalytic oxidation of formic acid: influence of metal particles composition on activity enhancement, Appl. Catal. B 221 (2018) 393–405.
[35] A. Shatla, K. Hassan, A. Abd-El-Latif, A. Hathoot, H. Baltruschat, M. Abdel-Azzem, Poly 1, 5 diaminonaphthalenes supported Pt, Pd, Pt/Pd and Pd/Pt nanoparticles for direct formic acid oxidation, J. Electroanal. Chem. 833 (2019) 231–241.
[36] M.J. Mostazo-López, D. Salinas-Torres, R. Ruiz-Rosas, E. Morallón, D. Cazorla-Amorós, Nitrogen-doped superporous activated carbons as electrocatalysts for the oxygen reduction reaction, Materials 12 (2019) 1346.
[37] O. Solorza-Feria, F.J.R. Varela, Pt and Pd-based electrocatalysts for ethanol and ethylene glycol fuel cells direct alcohol fuel cells, Springer 4 (2014) 63–78.
[38] Y. Sun, C. Du, G. Han, Y. Qu, L. Du, Y. Wang, G. Chen, Y. Gao, G. Yin, Boron, nitrogen co-doped graphene: superior electrocatalyst support and enhancing mechanism for methanol electrooxidation, Electrochim. Acta 212 (2016) 313–321.
[39] Z. Lei, M. Zhao, L. Dang, L. An, M. Lu, A.-Y. Lo, N. Yu, S.-B. Liu, Structural evolution and electrocatalytic application of nitrogen-doped carbon shells synthesized by pyrolysis of near-monodisperse polyaniline nanospheres, J. Mater. Chem. 19 (2009) 5985–5995.
[40] J.-H. Ma, L. Wang, X. Mu, L. Li, Nitrogen-doped graphene supported Pt nanoparticles with enhanced performance for methanol oxidation, Int. J. Hydrogen Energy 40 (2015) 2641–2647.
[41] H. Huang, L. Ma, C.S. Tiwary, Q. Jiang, K. Yin, W. Zhou, P.M. Ajayan, Worm-shape Pt nanocrystals grown on nitrogen-doped low-defect graphene sheets: highly efficient electrocatalysts for methanol oxidation reaction, Small 13 (2017) 1603013.
[42] K.K. Karuppanan, A.V. Raghu, M.K. Panthalingal, V. Thiruvenkatam, P. Karthikeyan, B. Pullithadathil, 3D-porous electrocatalytic foam based on Pt@N-doped graphene for high performance and durable polymer electrolyte membrane fuel cells, Sustain. Energy Fuels 3 (2019) 996–1011.
[43] S. Sankar, N. Watanabe, G.M. Anilkumar, B.N. Nair, S.G. Sivakamiammal, T. Tamaki, T. Yamaguchi, Electro-oxidation competency of palladium nanocatalysts over ceria–carbon composite supports during alkaline ethylene glycol oxidation, Catal. Sci. Technol. 9 (2019) 493–501.
[44] K.J. Ju, L. Liu, J.J. Feng, Q.L. Zhang, J. Wei, A.J. Wang, Bio-directed one-pot synthesis of Pt-Pd alloyed nanoflowers supported on reduced graphene oxide with enhanced catalytic activity for ethylene glycol oxidation, Electrochim. Acta 188 (2016) 696–703.